Analytical Forward Projection for Axial Non-Central Dioptric & Catadioptric Cameras

Amit Agrawal, Yuichi Taguchi, and Srikumar Ramalingam Mitsubishi Electric Research Labs (MERL), Cambridge, MA, USA

Abstract. We present a technique for modeling non-central catadioptric cameras consisting of a perspective camera and a rotationally symmetric conic reflector. While previous approaches use a central approximation and/or iterative methods for forward projection, we present an analytical solution. This allows computation of the optical path from a given 3D point to the given viewpoint by solving a 6th degree forward projection equation for general conic mirrors. For a spherical mirror, the forward projection reduces to a 4^{th} degree equation, resulting in a closed form solution. We also derive the forward projection equation for imaging through a refractive sphere (non-central dioptric camera) and show that it is a 10th degree equation. While central catadioptric cameras lead to conic epipolar curves, we show the existence of a quartic epipolar curve for catadioptric systems using a spherical mirror. The analytical forward projection leads to accurate and fast 3D reconstruction via bundle adjustment. Simulations and real results on single image sparse 3D reconstruction are presented. We demonstrate \sim 100 times speed up using the analytical solution over iterative forward projection for 3D reconstruction using spherical mirrors.

1 Introduction

Catadioptric cameras allow large field of view 3D reconstruction and stable egomotion estimation from few images. As analyzed in [1], there are only a few configurations that allow an effective single-viewpoint (central) catadioptric system. Simple mirrors such as sphere as well as configurations when the camera is not placed on the foci of hyperbolic/elliptical mirrors lead to a non-central system. To handle such configurations, it is important to accurately model a noncental catadioptric camera. Approximations using a central model could lead to inaccuracies such as skewed 3D estimation [2].

The projection of a scene point onto the image plane (Forward Projection) requires computing the light path from the scene point to the perspective camera's center of projection (COP). Thus, the reflection point on the mirror needs to be determined. This is considered to be hard problem and iterative solutions are usually employed assuming there are no closed form solutions. In this paper, we present an analytical solution to compute the forward projection (FP) for conic catadioptric systems, where the mirror is obtained by revolving a conic section around the axis of symmetry and the camera's COP is placed on the

mirror axis. We show that for a given 3D point, the mirror reflection point can be obtained by solving a 6^{th} degree equation for a general conic mirror. Interestingly, it reduces to solving a 4^{th} degree equation for a spherical mirror, resulting in a closed form solution. We show how to use these analytical solutions for fast 3D reconstruction using bundle adjustment, achieving a two order of magnitude speed up over previous approach [2].

Forward projection for imaging through a refractive sphere (non-central dioptric camera) is even more challenging due to two refractions. We show that the optical path from a given 3D point to a given viewpoint via a refractive sphere can be obtained by solving a 10^{th} degree equation. Thus, similar to mirrors, refractive spheres can also be used for 3D reconstruction by plugging its forward projection equation in a bundle adjustment algorithm. We believe that ours is the first paper to analyze this problem and derive a practical solution.

The epipolar geometry for central catadioptric systems (CCS) and for several non-central cameras (pushbroom, cross-slit, etc.) has been extensively studied. However, analyzing the epipolar geometry for non-central catadioptric cameras is difficult due to non-linear forward projection. We show the existence of a quartic epipolar curve for catadioptric systems employing spherical mirror. Contributions: Our paper makes the following contributions:

- We analyze forward projection for axial non-central dioptric/catadioptric cameras with conic reflectors and refractive spheres, and show that analytical solutions exist.
- We demonstrate that the back-projection for a spherical mirror can be formulated as a matrix-vector product and that the corresponding epipolar curves are quartic.
- We utilize the forward projection equations for fast sparse 3D reconstruction.

1.1 Related Work

Back-Projection and Epipolar Geometry: Baker and Nayar [1] presented the complete class of central catadioptric systems. Svoboda et al. [3, 4] studied the epipolar geometry for CCS and showed that the epipolar curves are conics. Geyer and Daniilidis [5] showed the existence of fundamental matrix for paracatadioptric cameras. A unified imaging model for all CCS was proposed by Geyer and Daniilidis [6]. Using this model for forward/back-projection with second order lifted image coordinates, Strum and Barreto [7] formulated the fundamental matrix for all CCS. For non-central cameras, Pless [8] introduced essential matrix for the calibrated case. Rademacher and Bishop [9] described epipolar curves for arbitrary non-central images. The epipolar geometry of cone-shaped mirrors, when restricted to planar motions was derived by Yagi and Kawato [10]. Spacek [11] described the epipolar geometry for two cameras mounted one on top of the other with aligned mirror axes.

Representing back-projection as a matrix-vector product for general mirrors is typically difficult. Several non-central cameras can be modeled by back-projection matrices operating on second order lifted image coordinates, result-

ing in conic epipolar curves. These include linear pushbroom cameras [12], linear oblique cameras [13], para-catadioptric cameras [14], and all general linear cameras (GLC) [15]. For the one-coefficient classical radial distortion model, the epipolar curves are cubic [16]. We show that for spherical mirror, back-projection can be described as matrix-vector product using *fourth order* lifted image coordinates, and thus the epipolar curves are quartic.

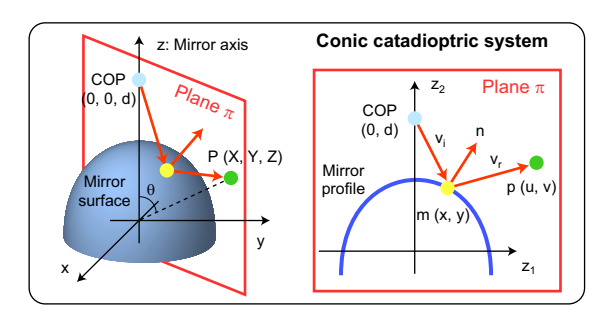
Forward projection for a non-central catadioptric camera is a hard problem, since the point on the mirror where the reflection happens need to be determined. In general, there is no closed-form solution for this problem, so non-linear optimization have been proposed (as in [17, 2]). Gonçalves and Nogueira [18] investigated quadric-shaped mirrors and reduced the problem to an optimization in a single variable. Baker and Nayar [1] were unable to find a closed form solution while analyzing mirror defocus blur and used numerical solutions. Their analysis was in 3D, since the finite camera aperture requires considering viewpoints not on the mirror axis. Vandeportaele [19] also analyzed forward projection for axial case, but in 3D using intersection of quadrics. In contrast, we derive a much simpler solution for the axial case in 2D with lower degree equation compared to [19].

Spherical mirrors have been used for visual servoing and wide-angle 3D reconstruction [20–22, 17, 2, 23]. Both [22] and [2] state that computing forward projection does not have a closed-form solution. In [22], a GLC approximation is used by tessellating the captured multi-perspective image into triangles and associating a GLC with each of them. In [2], an iterative method for forward projection is used. Interestingly, for spherical mirror, forward projection corresponds to the classical Alhazen's problem with four solutions [24]. We show that our FP equation for general quadric mirror reduces to a 4^{th} order equation for spherical mirror. Garg and Nayar [25] used a refractive sphere model for rain drops for generating near-perspective images (environment at infinity). However, they did not solve for the forward projection from a 3D point to compute the optical path, which we describe.

2 Forward Projection: Conic Reflectors

We first derive the forward projection equation for conic catadioptric systems. Let z axis be the mirror axis. A pinhole camera is placed at a distance d from the origin on the mirror axis. Let $P = [X, Y, Z]^T$ be a 3D scene point. Since the mirror is rotationally symmetric, the mirror reflection of P can be analyzed in the plane π containing the mirror axis and P (Figure 1 (left)). Let $(\mathbf{z}_1, \mathbf{z}_2)$ be the local coordinate system of π . In this plane, P has coordinates $\mathbf{p} = [u, v]^T$ given by $u = S \sin \theta$ and v = Z, where $S = \sqrt{X^2 + Y^2 + Z^2}$ is the distance of P from the origin and $\theta = \cos^{-1}(Z/S)$ is the angle between the mirror axis and the line joining the origin and the 3D point.

In plane π , the mirror is parameterized as a 2D conic $Az_2^2 + z_1^2 + Bz_2 = C$. This parametrization is used in [26] to handle spherical mirror along with other mirrors for computing the caustics. Let $\mathbf{m} = [x, y]^T$ be the reflection point on the



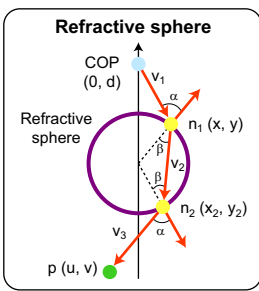


Fig. 1. (Left) Reflection for conic catadioptric systems can be analyzed in the plane π containing the mirror axis and the 3D scene point. (Right) Imaging through a refractive sphere can also be analyzed similarly.

mirror. Then $x = \pm \sqrt{C - By - Ay^2}$. The incident ray vector \mathbf{v}_i and the normal vector \mathbf{n} at \mathbf{m} are given by $\mathbf{v}_i = [x, y - d]^T$ and $\mathbf{n} = [x, B/2 + Ay]^T$. Using the law of reflection, the reflected ray vector $\mathbf{v}_r = \mathbf{v}_i - 2\mathbf{n}(\mathbf{n}^T\mathbf{v}_i)/(\mathbf{n}^T\mathbf{n})$. Since the reflected ray should pass through P, $\mathbf{v}_r \times (\mathbf{p} - \mathbf{m}) = 0$, where \times denotes the cross product. Solving using Matlab symbolic toolbox¹, we obtain a 6th order forward projection (FP) equation in y

$$u^{2}K_{1}^{2}(y) + K_{2}^{2}(y)(Ay^{2} + By - C) = 0,$$
(1)

where $K_1(y)$ and $K_2(y)$ are polynomials in y defined as

$$K_1(y) = K_{11}y^3 + K_{12}y^2 + K_{13}y + K_{14}, \quad K_2(y) = K_{21}y^2 + K_{22}y + K_{23}, \quad (2)$$

and the individual terms are given by

$$K_{11} = 4A(1 - A), \quad K_{12} = 4B - 4A(d + Ad + 2B)$$

$$K_{13} = 8AC - 4Bd - 3B^2 - 4C - 4ABd, \quad K_{14} = -dB^2 + 4CB + 4Cd$$

$$K_{21} = 4(A - 1)(A(d + v) + B), \quad K_{22} = 8C + 2B^2 + 4A(-2C + B(d + v) + 2dv)$$

$$K_{23} = B^2(d + v) + 4B(-C + dv) - 4C(v + d).$$

For a given P, solving (1) results in six solutions for y. The correct solution can be found by checking the law of reflection for each real solution. Note that for the correct solution $\mathbf{v}_r^T \mathbf{n} = -\mathbf{v}_i^T \mathbf{n}$. Using $x = \text{sign}(u) \sqrt{C - By - Ay^2}$, the 3D mirror reflection point can be obtained as $x\mathbf{z}_1/\|\mathbf{z}_1\| + y\mathbf{z}_2/\|\mathbf{z}_2\|$.

Spherical Mirror: Substituting $A = 1, B = 0, C = r^2$, where r is the mirror radius, results in a 4^{th} order forward projection equation

$$u^{2}(r^{2}(d+y) - 2dy^{2})^{2} - (r^{2} - y^{2})(r^{2}(d+v) - 2dvy)^{2} = 0.$$
 (3)

Thus, a close form solution for y can be obtained. Notice that for a spherical mirror, the pinhole location is not restricted. For any pinhole location, a new axis

 $^{^{1}}$ Matlab code and intermediate steps are provided in the supplementary materials.

Mirror Shape	Pinhole Placement	Parameters	Central System	Degree
General	On axis	A,B,C	No	6
Sphere	Any	A=1,B=0,C>0	No	4
Elliptic	On axis, At Foci	B = 0	Yes	2
Elliptic	On axis, Not at Foci	B = 0	No	6
Hyperbolic	On axis, At Foci	A < 0, C < 0	Yes	2
Hyperbolic	On axis, Not at Foci	A < 0, C < 0	No	6
Parabolic	On axis, $d = \infty$	A = 0, C = 0	Yes	2
Parabolic	On axis, Finite d	A = 0, C = 0	No	5

Table 1. Degree of forward projection equation for central and non-central catadioptric systems using conic reflectors.

joining the pinhole and the sphere center can be defined. In all other cases, the pinhole needs to be on the mirror axis. Table 1 shows the degree of FP equation for spherical (A=1,B=0,C>0), elliptical (B=0), hyperbolic (A<0,C<0) and parabolic (A=0,C=0) mirrors. Note that when the catadioptric system is central, the degree of FP is two. This is intuitive, since the reflection point can be obtained by intersecting the mirror with the ray joining the 3D point and the effective projection center.

3 Back-Projection & Epipolar Curve for Spherical Mirror

Now we show that back-projection equations for a non-central catadioptric system using a spherical mirror can be written in matrix-vector form. By intersecting the back-projected ray with a general 3D ray, we show the existence of a quartic epipolar curve. Then we verify that the projection of points on the same 3D line onto the image plane using the FP equation results in the same curve.

Let $\mathbf{C}_p = [0, 0, -d]^T$ be the COP and let the spherical mirror of radius r be located at the origin (Figure 2 (left)). For an image point \mathbf{q} , let $\mathbf{s} = K^{-1}\mathbf{q}$ be the ray direction, where $K_{3\times 3}$ is the internal camera calibration matrix. The intersection points \mathbf{b} with the mirror are given by

$$\mathbf{b} = \mathbf{C}_p + \mathbf{s} \frac{ds_3 \pm \sqrt{d^2 s_3^2 - (d^2 - r^2)(\mathbf{s}^T \mathbf{s})}}{\mathbf{s}^T \mathbf{s}},$$
 (4)

where s_3 is the third element of **s**. Note that $\mathbf{b}^T \mathbf{b} = r^2$ and the normal at **b** is \mathbf{b}/r . Since $\mathbf{v}_i = \mathbf{b} - \mathbf{C}_p$, the reflected vector \mathbf{v}_r is given by

$$\mathbf{v}_r = (\mathbf{b} - \mathbf{C}_p) - 2\mathbf{b}(\mathbf{b}^T(\mathbf{b} - \mathbf{C}_p))/r^2 = -\mathbf{b} - \mathbf{C}_p + 2\mathbf{b}(\mathbf{b}^T\mathbf{C}_p)/r^2, \quad (5)$$

which intersects the mirror axis at $\mathbf{m} = [0, 0, k]^T$, where $k = dr^2/(2db_3 + r^2)$. Thus, the Plücker coordinates of the reflected 3D ray are given by $\mathbf{L} = (\mathbf{b}^T - \mathbf{m}^T, (\mathbf{b} \times \mathbf{m})^T)^T$, where \times denotes the cross product. Similar to [7], we use \mathbf{L}_+ and \mathbf{L}_- to represent the reflected rays corresponding to the two intersections of

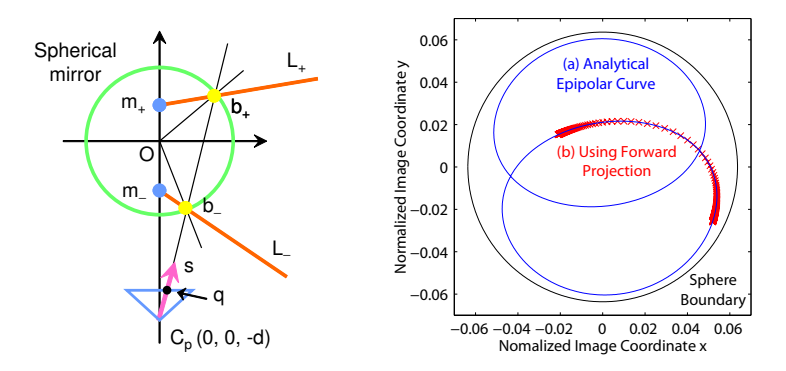


Fig. 2. (Left) Depicting back-projection. (Right) Epipolar curves, analytically computed by Equation (8) (a) and numerically computed by using the FP equation (b) for a known 3D line match.

 \mathbf{v}_i with the sphere (\mathbf{b}_+ and \mathbf{b}_-). We represent the two lines with a second-order line complex \mathbf{C} , described as a symmetric 6×6 matrix

$$\mathbf{C} \sim W(\mathbf{L}_{+}\mathbf{L}_{-}^{T} + \mathbf{L}_{-}\mathbf{L}_{+}^{T})W, \quad W = \begin{pmatrix} 0 & I \\ I & 0 \end{pmatrix}, \tag{6}$$

where \sim denotes the equality of matrices up to a scale factor. By substituting **b** and **m**, we obtain a line complex **C** that includes *quartic* monomials of **s**. As in [7], let $\mathbf{v}_{sym}(\mathbf{C})$ be the column-wise vectorization of the upper-right triangular part of **C** (21-vector) and $\hat{\mathbf{s}}$ denote *double lifted* coordinates of **s** in the lexicographic order (15-vector). Then we obtain the back-projection equation in a matrix-vector form:

$$\mathbf{v}_{sym}(\mathbf{C}) \sim B_{r,d}\hat{\hat{\mathbf{s}}} = B_{r,d}\hat{\hat{K}}^{-1}\hat{\hat{\mathbf{q}}}, \tag{7}$$

where $B_{r,d}$ is a sparse 21×15 matrix depending only on r and d, as shown in the supplementary materials.

Note that the difference between [7] and ours is that $\mathbf{m} = [0, 0, 0]$ in [7], since the reflected ray passes through the *center* of an imaginary sphere that models all central catadioptric systems [6]. For a non-central catadioptric system, \mathbf{m} becomes dependent on the image pixel \mathbf{q} . Note that when the pinhole is on the mirror axis, one can always find the intersection point \mathbf{m} as [0,0,k] for some k. **Epipolar Curve**: Consider a 3D ray defined in the sphere-centered coordinate system and represented with Plücker coordinates as \mathbf{L}_0 . This ray intersects the line complex \mathbf{C} iff

$$\mathbf{L}_0^T \mathbf{C} \mathbf{L}_0 = 0. \tag{8}$$

Since C includes quartic monomials of \mathbf{s} (thus \mathbf{q}), the constraint results in a 4^{th} order curve. The projection of \mathbf{L}_0 therefore appears as a quartic curve in the image of spherical mirror, which means that spherical-mirror based catadioptric systems yield quartic epipolar curves. Our FP equation allows us to validate the

degree and shape of epipolar curves. Figure 2 (right) compares the epipolar curve analytically computed from (8) with the curve obtained by projecting 3D points on \mathbf{L}_0 using the FP equation. We can observe that the shape of curves agree and the numerical curve (using FP) is a continuous section of the analytical quartic curve. Note that the image point converges as the 3D point goes to $\pm \infty$ on \mathbf{L}_0 .

Similar to perspective cameras, the quartic epipolar curve can be used to restrict the search space for dense stereo matching. Typically, approximations such as epsilon-stereo constraint [22] are used, which assumes that the corresponding match will lie approximately along a line. However, our analysis provides the analytical 2D epipolar curve for non-central spherical mirror cameras. Note that the FP equation for general conic mirrors simplifies the correspondence search for other non-central conic catadioptric systems as well.

4 Sparse 3D Reconstruction using Spherical Mirrors

We demonstrate the applicability of analytical forward projection (AFP) for sparse 3D reconstruction using well-known bundle adjustment algorithm, and compare it with iterative forward projection (IFP) method [2]. We choose a simpler setup of a single perspective camera imaging multiple spherical mirrors as shown in Figure 4. We assume that the internal camera calibration is done separately (off-line) and the sphere radius is known (we used high sphericity stainless steel balls as spherical mirrors for real experiments). Thus, our optimization involves estimating the sphere centers and the 3D points in the camera coordinate system. Note that the FP equation can be easily applied to more general calibration/3D reconstruction involving rotationally symmetric setups with parabolic/hyperbolic mirrors [2]. For moving camera+mirror system, one may require a central approximation to get the initial estimate of the relative camera motion. However, AFP can replace IFP in subsequent bundle adjustment. In addition, since AFP leads to a fast algorithm, we demonstrate in Section 4.3 that a central approximation is not required for iterative outlier removal.

4.1 Bundle Adjustment for Spherical Mirror using AFP

Let $\mathbf{C}(i) = \begin{bmatrix} C_x(i), C_y(i), C_z(i) \end{bmatrix}^T$, $i = 1 \dots M$ be the sphere centers and $\mathbf{P}(j) = \begin{bmatrix} P_x(j), P_y(j), P_z(j) \end{bmatrix}^T$, $j = 1 \dots N$ be the 3D points in the camera coordinate system, when the pinhole camera is placed at the origin. First we rewrite the FP equation (3) in terms of 3D quantities. For a given 3D point $\mathbf{P}(j)$ and mirror center $\mathbf{C}(i)$, the orthogonal vectors \mathbf{z}_1 and \mathbf{z}_2 defining plane π are given by $\mathbf{z}_2 = -\mathbf{C}(i)$ and $\mathbf{z}_1 = \mathbf{P}(j) - \mathbf{C}(i) \frac{\mathbf{C}(i)^T \mathbf{P}(j)}{\|\mathbf{C}(i)\|^2}$. Further, $d = \|\mathbf{z}_2\|$, $u = \|\mathbf{z}_1\|$, and $v = -\mathbf{C}(i)^T (\mathbf{P}(j) - \mathbf{C}(i)) / \|\mathbf{C}(i)\|$. By substituting d, u and v in (3), the FP equation can be re-written as

$$c_1 y^4 + c_2 y^3 + c_3 y^2 + c_4 y + c_5 = 0, (9)$$

where each coefficient c_i becomes a function of $\mathbf{P}(j)$ and $\mathbf{C}(i)$ only. In general, when the scene point is outside the sphere and is visible through mirror reflection,

there are four real solutions. The single correct solution is found by checking the law of reflection for each of them.

Using the solution, the 3D reflection point on the sphere is obtained as

$$\mathbf{R}_{m}(i,j) = \left[X_{m}(i,j), Y_{m}(i,j), Z_{m}(i,j)\right]^{T} = \mathbf{C}(i) + \sqrt{r^{2} - y^{2}} \frac{\mathbf{z}_{1}}{\|\mathbf{z}_{1}\|} + y \frac{\mathbf{z}_{2}}{\|\mathbf{z}_{2}\|}.$$
(10)

Finally, the 2D image projection pixel is obtained as $p(i,j) = \frac{f_x X_m(i,j)}{Z_m(i,j)} + c_x$, $q(i,j) = \frac{f_y Y_m(i,j)}{Z_m(i,j)} + c_y$, where (f_x, f_y) and (c_x, c_y) are the focal length and the principal point of the camera, respectively.

Let $[\hat{p}(i,j), \hat{q}(i,j)]^T$ be the image projection of the j^{th} 3D point for the i^{th}

Let $[\hat{p}(i,j), \hat{q}(i,j)]^T$ be the image projection of the j^{th} 3D point for the i^{th} sphere and $[p(i,j),q(i,j)]^T$ denote their current estimates, computed from the current estimates of sphere centers and 3D scene points. Each pair (i,j) gives a 2-vector error function $F(i,j) = [p(i,j) - \hat{p}(i,j), q(i,j) - \hat{q}(i,j)]^T$, and the average reprojection error is given by $E = \frac{1}{NM} \sum_{j=1}^{N} \sum_{i=1}^{M} \|F(i,j)\|^2$. We perform bundle adjustment by minimizing E (using Matlab function lsqnonlin), starting from an initial solution. The initial 3D points are obtained as the center of the shortest transversal of the respective back-projection rays. The initial sphere centers are perturbed from their true positions (simulations) and obtained using the captured photo (real experiments).

Jacobian Computation: AFP also enables the analytical Jacobian computation, which speeds up bundle adjustment. Let t denote an unknown. Then

$$\frac{\partial F(i,j)}{\partial t} = \begin{bmatrix} \frac{\partial p(i,j)}{\partial t} \\ \frac{\partial q(i,j)}{\partial t} \end{bmatrix} = \begin{bmatrix} f_x(\frac{1}{Z_m(i,j)} \frac{\partial X_m(i,j)}{\partial t} - \frac{X_m(i,j)}{Z_m(i,j)^2} \frac{\partial Z_m(i,j)}{\partial t}) \\ f_y(\frac{1}{Z_m(i,j)} \frac{\partial Y_m(i,j)}{\partial t} - \frac{Y_m(i,j)}{Z_m(i,j)^2} \frac{\partial Z_m(i,j)}{\partial t}) \end{bmatrix}.$$
(11)

Since X_m, Y_m, Z_m depend on y, the above derivatives depend on $\frac{\partial y}{\partial t}$. Typically, one would assume that a closed form expression for y is required to compute $\frac{\partial y}{\partial t}$. However, it can be avoided by taking the derivative of the FP equation (9) as

$$\frac{\partial y}{\partial t} = -\frac{y^4 \frac{\partial c_1}{\partial t} + y^3 \frac{\partial c_2}{\partial t} + y^2 \frac{\partial c_3}{\partial t} + y \frac{\partial c_4}{\partial t} + \frac{\partial c_5}{\partial t}}{4c_1 y^3 + 3c_2 y^2 + 2c_3 y + c_4}.$$
 (12)

For a given 3D point $\mathbf{P}(j)$ and sphere center $\mathbf{C}(i)$, y can be computed by solving the FP equation and thus can be substituted in above to obtain $\frac{\partial y}{\partial t}$. The gradient of the reprojection error with respect to each unknown can be obtained using Equations (10),(11), and (12). Thus, we showed that the analytical FP equation can be used to compute the Jacobian of the reprojection error, without obtaining a closed-form solution for the mirror reflection point.

4.2 Simulations

We place a pinhole camera at the center of the coordinate system and M=4 spheres (radius r=0.5") at a distance of 200 mm. N=100 3D points were randomly distributed in a hemisphere of radius 1000 mm surrounding the spheres

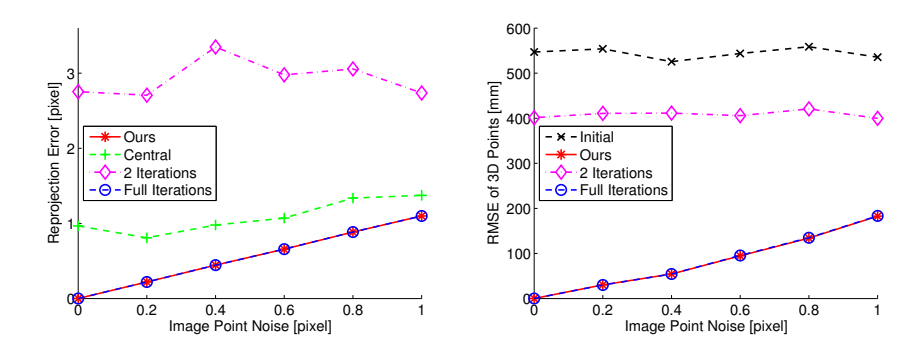


Fig. 3. Bundle adjustment simulations using M=4 spherical mirrors and N=100 3D points for different image noise levels. (Left) Reprojection error. (Right) RMSE of reconstructed 3D points. The IFP curve matches the AFP curve when sufficient iterations are used.

Table 2. Comparison of bundle adjustment run time (in seconds) using IFP [2] and our AFP for N 3D points and M=4 spherical mirrors. The run times were obtained by repeating bundle adjustment 20 times and averaging.

ſ	Run Time	Iterative FP	AFP (Without Jacobian)	AFP (With Jacobian)
ſ	N = 100	470	6.6	4.0
	N = 1000	4200	68	48

and their true image projections were computed using the FP equation. Gaussian noise was added both to sphere centers ($\sigma=0.5$ mm) and true image projections ($\sigma=[0-1]$ pixels). We compare the reconstruction error using (a) AFP, (b) central approximation (the projection center was fixed at 0.64r mm from the sphere center as in [2]), and (c) IFP [2]. IFP first computes the initial image projection of a 3D point using the central approximation and then performs non-linear optimization to minimize the distance between the 3D point and the back-projected ray. It required ~ 5 iterations to converge in the simulations.

Figure 3 compares the reprojection error and the root mean square error (RMSE) in 3D points for different image noise levels. Note that only when sufficient iterations are performed for IFP (referred to as 'full iterations'), its error reduces to that of AFP (same curve). The central approximation or smaller number of iterations for IFP lead to larger errors. In Figure 3 (right), the error due to central approximation is too large $(1.5 \times 10^4 \text{ mm})$ to be shown in the graph.

Run time for projecting 10^5 3D points with a single sphere was 1120 seconds for IFP (full iterations) and 13.8 seconds for AFP (\sim 80 times faster). Table 2 compares the bundle adjustment run time, which shows that AFP along with analytical Jacobian computation achieves a speed up of \sim 100. While the number of iterations in bundle adjustment was almost the same for IFP and AFP, IFP takes much longer time due to iterative optical path computation for each 3D point and mirror pair. Similar speed-ups were obtained for elliptic, hyperbolic,



Fig. 4. Input images (left) and zoom-in of sphere images (middle and right) superimposed with extracted SIFT features. Red dots and green crosses respectively represent inliers and outliers determined in the iterative bundle adjustment process. Top shows rendered image using POV-Ray and bottom shows real photo captured using a camera.

and parabolic mirrors as well (projecting 10^5 3D points took 1600–1800 seconds for IFP and 22 seconds for AFP).

4.3 POV-Ray Simulations and Real Results using Feature Matching

In practice, the corresponding image points are estimated using a feature matching algorithm such as SIFT, and invariably contain outliers and false matches. We first show results using SIFT on sphere images rendered using POV-Ray, which allows performance evaluation using available ground truth data.

Figure 4 (top) shows a rendered image (resolution 2000×2000) of four spherical mirrors, placed at the center of a cube 1000mm on each side. The walls of the cube consist of textured planes. We extract SIFT features and select corresponding points that are consistent among the four sphere images. For initial sphere centers, we add Gaussian noise ($\sigma=0.3$ mm) to their ground truth locations. Since the SIFT matches contains outliers, we perform robust reconstruction by iterating bundle adjustment with outlier removal. After each bundle adjustment step, we remove all 3D points whose reprojection error is greater than twice the average reprojection error. Figure 5 shows that by iterating bundle adjustment and outlier removal, the reprojection error and RMSE of 3D points reduces significantly for all planes (from ~ 460 mm to 6 mm). Figure 5 also shows the number of inliers after each bundle adjustment step. Note that since AFP significantly reduces bundle adjustment time, this simple procedure can be repeated multiple times and is effective in handling outliers.

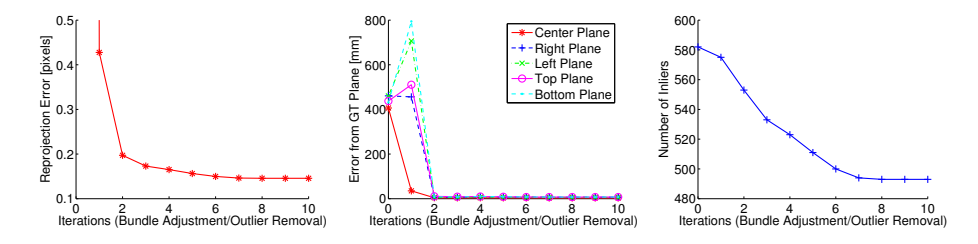


Fig. 5. 3D reconstruction results for the POV-Ray data. (Left) Reprojection error. (Middle) Average distance of reconstructed 3D points from the ground-truth (GT) planes. (Right) Number of inliers after each bundle adjustment/outlier removal step.

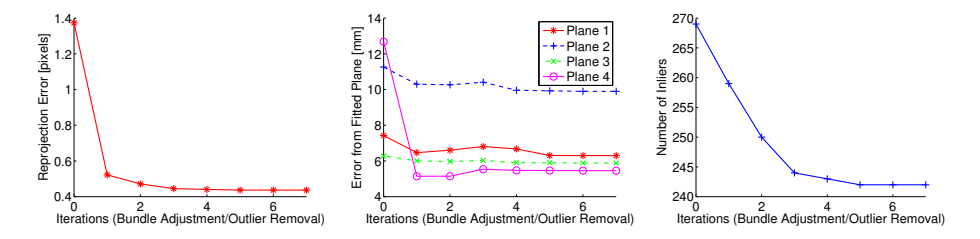


Fig. 6. 3D reconstruction results for the real data. (Left) Reprojection error. (Middle) Average distance of reconstructed 3D points from their fitted planes. (Right) Number of inliers after each bundle adjustment/outlier removal step.

Real Results: We used four spherical mirrors (radius 0.75") placed with an interval of 3", and captured a single photo using a Mamiya 645AFD camera, as shown in Figure 4 (bottom). Each sphere image in the captured photo has 1300×1300 resolution. To determine initial sphere centers, we mark several points on each sphere boundary, corresponding to the rays tangential to the sphere. We find the central ray that makes the same angle α with all the tangential rays. The sphere center is then at a distance of $\frac{r}{\sin\alpha}$ along the central ray. Figure 6 shows the reconstruction results. Since the ground truth is not available, we fit planes to the set of 3D points corresponding to each plane in the scene (Planes 1–4 in Figure 4) and measure the average distance error of the 3D points from the plane. Note that this error measure includes a bias, but validates that the reconstructed 3D points are aligned on a plane with small errors (Figure 6 (middle)).

5 Forward Projection for Refractive Sphere

Now we derive the forward projection equation for imaging through a refractive sphere, which results in a non-central dioptric system. The key idea is to use the vector equation of the refracted ray [27], instead of directly applying Snell's law.

Let a refractive sphere of radius r and constant refractive index μ be placed at the origin of the coordinate system. Let the COP be at distance d from the origin. As before, we consider the plane containing the optical axis and the scene

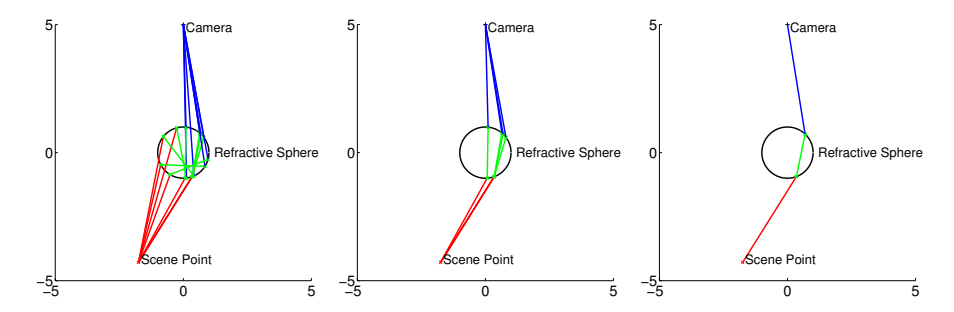


Fig. 7. Solving the FP equation for a refractive sphere with r = 1, $\mu = 1.5$ and d = 5. (Left) 8 real solutions. (Middle) 4 solutions after constraining $y \ge r^2/d$. (Right) Correct solution after testing Snell's law.

point P. Let $\mathbf{n}_1 = [x, y]^T$ and $\mathbf{n}_2 = [x_2, y_2]^T$ be refraction points on the sphere, and $v_1 \to v_2 \to v_3$ represent the optical path from COP to P (Figure 1 (right)). Then $\mathbf{v}_1 = [x, y - d]^T$ and $\mathbf{n}_1^T \mathbf{n}_1 = \mathbf{n}_2^T \mathbf{n}_2 = r^2$. Given an incoming ray \mathbf{v}_i and normal \mathbf{n} at a surface separating mediums of refractive index μ_1 and μ_2 , the refracted ray \mathbf{v}_r can be written in vector form [27] as $\mathbf{v}_r = a\mathbf{v}_i + b\mathbf{n}$, where

$$a = \frac{\mu_1}{\mu_2}, \quad b = \frac{-\mu_1 \mathbf{v}_i^T \mathbf{n} \pm \sqrt{\mu_1^2 (\mathbf{v}_i^T \mathbf{n})^2 - (\mu_1^2 - \mu_2^2) (\mathbf{v}_i^T \mathbf{v}_i) (\mathbf{n}^T \mathbf{n})}}{\mu_2 (\mathbf{n}^T \mathbf{n})}.$$
 (13)

This gives $\mathbf{v}_r^T \mathbf{n} \propto \pm \sqrt{\mu_1^2 (\mathbf{v}_i^T \mathbf{n})^2 - (\mu_1^2 - \mu_2^2) (\mathbf{v}_i^T \mathbf{v}_i) (\mathbf{n}^T \mathbf{n})}$. The correct sign is obtained by using the constraint that the signs of $\mathbf{v}_r^T \mathbf{n}$ and $\mathbf{v}_i^T \mathbf{n}$ should be the same. Since the tangent ray from COP to the sphere occurs at $y = r^2/d$, $y \ge r^2/d$ for valid refraction point. This gives $\mathbf{v}_1^T \mathbf{n}_1 = r^2 - dy \le 0$. Thus,

$$\mathbf{v}_{2} = \frac{1}{\mu} \mathbf{v}_{1} + \mathbf{n}_{1} \frac{-\mathbf{v}_{1}^{T} \mathbf{n}_{1} - \sqrt{(\mathbf{v}_{1}^{T} \mathbf{n}_{1})^{2} - r^{2}(1 - \mu^{2})(\mathbf{v}_{1}^{T} \mathbf{v}_{1})}}{\mu r^{2}}.$$
 (14)

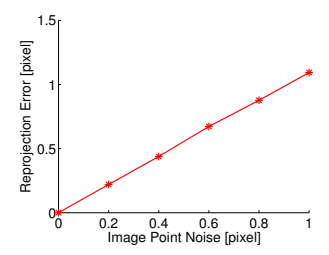
The second refraction point \mathbf{n}_2 can be written as $\mathbf{n}_1 + \lambda \mathbf{v}_2$ for some constant λ , which can be obtained as follows.

$$r^{2} = \mathbf{n}_{2}^{T} \mathbf{n}_{2} = r^{2} + \lambda^{2} \mathbf{v}_{2}^{T} \mathbf{v}_{2} + 2\lambda \mathbf{v}_{2}^{T} \mathbf{n}_{1}, \quad \Rightarrow \lambda = -2\mathbf{v}_{2}^{T} \mathbf{n}_{1} / \mathbf{v}_{2}^{T} \mathbf{v}_{2}. \tag{15}$$

The outgoing refracted ray is given by $\mathbf{v}_3 = \mu \mathbf{v}_2 + b_3 \mathbf{n}_2$, for some b_3 . Note that the symmetry of sphere results in $\mathbf{v}_3^T \mathbf{n}_2 = -\mathbf{v}_1^T \mathbf{n}_1$ and $\mathbf{v}_2^T \mathbf{n}_2 = -\mathbf{v}_2^T \mathbf{n}_1$. Using these constraints, b_3 is obtained as $b_3 = (-\mathbf{v}_1^T \mathbf{n}_1 - \mu \mathbf{v}_2^T \mathbf{n}_1)/r^2$. Finally, the outgoing refracted ray \mathbf{v}_3 should pass through the scene point $\mathbf{p} = [u, v]^T$. Thus, $\mathbf{v}_3 \times (\mathbf{p} - \mathbf{n}_2) = 0$. By substituting all the terms, we get

$$0 = \mathbf{v}_3 \times (\mathbf{p} - \mathbf{n}_2) \quad \Rightarrow 0 = K_1(x, y) + K_2(x, y)\sqrt{A} + K_3(x, y)A^{3/2}, \quad (16)$$

where $A = d^2\mu^2r^2 - d^2x^2 - 2d\mu^2r^2y + \mu^2r^4$, and K_1 , K_2 and K_3 are polynomials in x and y (provided in the supplementary materials with Matlab code). After



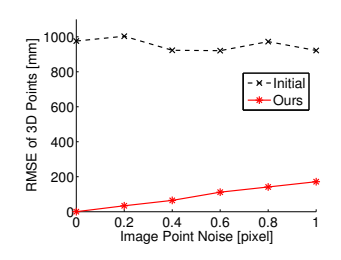


Fig. 8. Bundle adjustment simulations using M=4 refractive spheres and N=100 3D points for different image noise levels. (Left) Reprojection error. (Right) RMSE of reconstructed 3D points.

removing the square root terms, substituting $x^2 = r^2 - y^2$ and simplifying, we finally obtain a 10^{th} degree equation in y.

Figure 7 shows an example of solving the FP equation for refractive sphere. In general, when the 3D point is not on the axis, only 8 out of 10 solutions are real. Constraining $y \geq r^2/d$ further reduces to 4 solutions and the correct solution is found by testing the Snell's law for each of them. Figure 8 demonstrates that the FP equation can be used in a bundle adjustment algorithm for sparse 3D reconstruction using refractive spheres, similar to catadioptric systems.

6 Discussions and Conclusions

We believe that our paper advances the field of catadioptric imaging both theoretically and practically. Theoretically, we have derived analytical equations of forward projection for a broad class of non-central catadioptric cameras and have shown existence of quartic epipolar curves for spherical-mirror based catadioptric systems. We hope that our work will lead to further geometric analysis of non-central catadioptric cameras for mirror defocus, epipolar geometry, and wide-angle sparse as well as dense 3D reconstruction. Practically, the analytical FP and Jacobian computation significantly reduce the bundle adjustment run time. Thus, the computational complexity of using a non-central model becomes similar to that of a central approximation. The FP equation may be useful for reducing the search space in dense stereo matching and for auto-calibration via projection of scene features such as lines. We have also shown sparse 3D reconstruction using a dioptric non-central camera with refractive spheres, by deriving its forward projection equation. Unlike a catadioptric system, the camera is not visible in the captured image for a refractive setup. This could be a benefit in certain wide-angle applications, replacing expensive fish-eye lenses.

Acknowledgments. We thank the anonymous reviewers for their feedback and Peter Sturm for referring us to [19]. We also thank Jay Thornton, Keisuke Kojima, John Barnwell, and Haruhisa Okuda, Mitsubishi Electric, Japan, for their help and support.

References

- Baker, S., Nayar, S.: A theory of single-viewpoint catadioptric image formation. IJCV 35 (1999) 175–196
- Micusik, B., Pajdla, T.: Autocalibration and 3D reconstruction with non-central catadioptric cameras. In: CVPR. (2004) 58–65
- Svoboda, T., Pajdla, T.: Epipolar geometry for central catadioptric cameras. IJCV 49 (2002) 23–37
- Svoboda, T., Pajdla, T., Hlavac, V.: Epipolar geometry for panoramic cameras. In: ECCV. Volume 1. (1998) 218–231
- Geyer, C., Daniilidis, K.: Properties of the catadioptric fundamental matrix. In: ECCV. (2002) 140–154
- 6. Geyer, C., Daniilidis, K.: A unifying theory of central panoramic systems and practical implications. In: ECCV. (2000) 159–179
- Sturm, P., Barreto, J.P.: General imaging geometry for central catadioptric cameras. In: ECCV. Volume 4. (2008) 609

 –622
- 8. Pless, R.: Using many cameras as one. In: CVPR. (2003) 587-594
- Rademacher, P., Bishop, G.: Multiple-center-of-projection images. In: SIG-GRAPH. (1998) 199–206
- Yagi, Y., Kawato, S.: Panoramic scene analysis with conic projection. In: Proc. IEEE Int'l Workshop on Intelligent Robots and Systems. (1990) 181–187
- 11. Spacek, L.: Coaxial omnidirectional stereopsis. In: ECCV. (2004) 354-365
- 12. Gupta, R., Hartley, R.: Linear pushbroom cameras. PAMI 19 (1997) 963-975
- 13. Pajdla, T.: Stereo with oblique cameras. IJCV 47 (2002) 161–170
- Geyer, C., Daniilidis, K.: Paracatadioptric camera calibration. PAMI 24 (2002) 687–695
- 15. Yu, J., McMillan, L.: General linear cameras. In: ECCV. (2004)
- 16. Zhang, Z.: On the epipolar geometry between two images with lens distortion. In: ICPR. Volume 1. (1996) 407–411
- Micusik, B., Pajdla, T.: Structure from motion with wide circular field of view cameras. PAMI 28 (2006) 1135–1149
- Gonçalvez, N., Nogueira, A.C.: Projection through quadric mirrors made faster. In: OMNIVIS. (2009)
- 19. Vandeportaele, B.: Contributions à la vision omnidirectionnelle : Etude, Conception et Étalonnage de capteurs pour lacquisition dimages et la modélisation 3D. PhD thesis, Institut National Polytechnique de Toulouse, France (2006) in french.
- Hong, J., Tan, X., Pinette, B., Weiss, R., Riseman, E.: Image-based homing. In: ICRA. (1991) 620–625
- 21. Lanman, D., Crispell, D., Wachs, M., Taubin, G.: Spherical catadioptric arrays: Construction, multi-view geometry, and calibration. In: 3DPVT. (2006) 81–88
- 22. Ding, Y., Yu, J., Sturm, P.: Multi-perspective stereo matching and volumetric reconstruction. In: ICCV. (2009)
- Kojima, Y., Sagawa, R., Echigo, T., Yagi, Y.: Calibration and performance evaluation of omnidirectional sensor with compound spherical mirrors. In: OMNIVIS. (2005)
- 24. Glaeser, G.: Reflections on spheres and cylinders of revolution. J. Geometry and Graphics 3 (1999) 121–139
- 25. Garg, K., Nayar, S.K.: Vision and rain. IJCV 75 (2007) 3-27
- Swaminathan, R., Grossberg, M., Nayar, S.: Non-single viewpoint catadioptric cameras: Geometry and analysis. IJCV 66 (2006) 211–229
- 27. Glassner, A.S., ed.: An introduction to ray tracing. Academic Press Ltd. (1989)